Supporting information

Thin Stencil Membrane-Assisted High Throughput Single-Cell to Cluster of Cells Micropatterning and Large-Size Biomolecular Transfection in Primary and Stem Cells

Donia Dominic[a], Srabani Kar[a, b], Rajdeep Ojha[c], Moeto Nagai[d], Tuhin Subhra Santra[a,e*]

[a]Department of Engineering Design, Indian Institute of Technology Madras, India
[b]Department of Physics, Indian Institute of Technology, Hyderabad, India
[c]Department of Physical Medicine and Rehabilitation, Christian Medical College, India
[d]Department of Mechanical Engineering, Toyohashi University of Technology, Japan
[e]School of Interdisciplinary Studies, Indian Institute of Technology Madras, India

Corresponding author: Tuhin Subhra Santra, tuhin@smail.iitm.ac.in, santra.tuhin@gmail.com

Table S1 Comparison of different cell patterning methods for their patterning efficiency

Method	**Pattern size**	**Cell patterning efficiency (%)**	**Single-cell patterning efficiency**	**Reference**
Ultrathin metal microstencil	23–25 µm holes	Not explicitly stated	~88% single-cell occupancy (per total patterned sites)	[1]
Microfabricated elastomeric PDMS stencil	10–50 µm holes (various shapes)	Qualitative (efficient patterning)	Not quantified	[2]
PDMS micropillar/protein island stamp	40, 60, 80, 100 µm patterns	97–99.7% (best case, 100 µm)	~70–90% (size-dependent)	[3]
Ultrathin SU-8 microstencil membrane	40–80 µm holes	80.5% (L929)	75.8% (per *occupied* sites)	[4]
Photopatterned hydrogel cell islands	80 × 80 µm	94.4%	54.2% (per *occupied* sites)	[5,6]
Microwells + paired protein patterns	40 µm wells	~79.8% (best case)	86.4% (per *occupied* sites)	[6]
Hydrodynamic guiding microwells	~15 µm features	>80%	>64%	[7]

Table S2: Detailed comparative analysis with prior works.

Feature	**Microcontact printing[3]**	**Su-8 Membrane[4]**	**Micropore array chip[8]**	**Our work**
Patterning method	PDMS microcontact	SU-8 membrane	Micropore array (vacuum	PDMS stencil

	printing		trapping)	
Lowest cell micropattern dimension	40 μm	45 μm	2-5 μm	25 μm
Cluster cell patterning efficiency for the highest pattern dimension	~97–99% (100 μm)	NA	NA	100% (100 μm)
Cluster cell Patterning efficiency for the lowest pattern dimension	~63-72% (40 μm)	~80–95%	NA	92-96% (40 μm)
Single-cell efficiency definition	Patterns occupied by single cells / Total cell *occupied patterns*	Patterns occupied by single cells / Total cell *occupied patterns*	Patterns occupied by single cells / Total cell *occupied patterns*	Patterns occupied by single cells / Total number of *patterns*
Single-cell patterning efficiency	~53-72% (40 μm)	Tunable(5%-76%)(45 μm)	~66–75%	~78-90% (25 μm)
Delivery method	Laser + titanium micro-dish (photoporation)	Laser+ Titanium micro ring device (photoporation)	Electroporation	Laser+ rGO (photoporation)
Delivery efficiency	~92% - 98%	~95% - 97%	>90%	~72-93%
Cell viability	~95% - 99%	~98% - 100%	>90%	~85-96%
Fabrication complexity	High	High	Very High (microfabrication + microfluidics)	Low
Material system	Titanium	SU-8 + Titanium	Silicon/polymer chip	PDMS + rGO
Flexibility/adaptability	Low	low	Lowest (fixed geometry)	High
Biological applicability	Moderate	Moderate	low (constrained cells)	High (primary/stem cells)

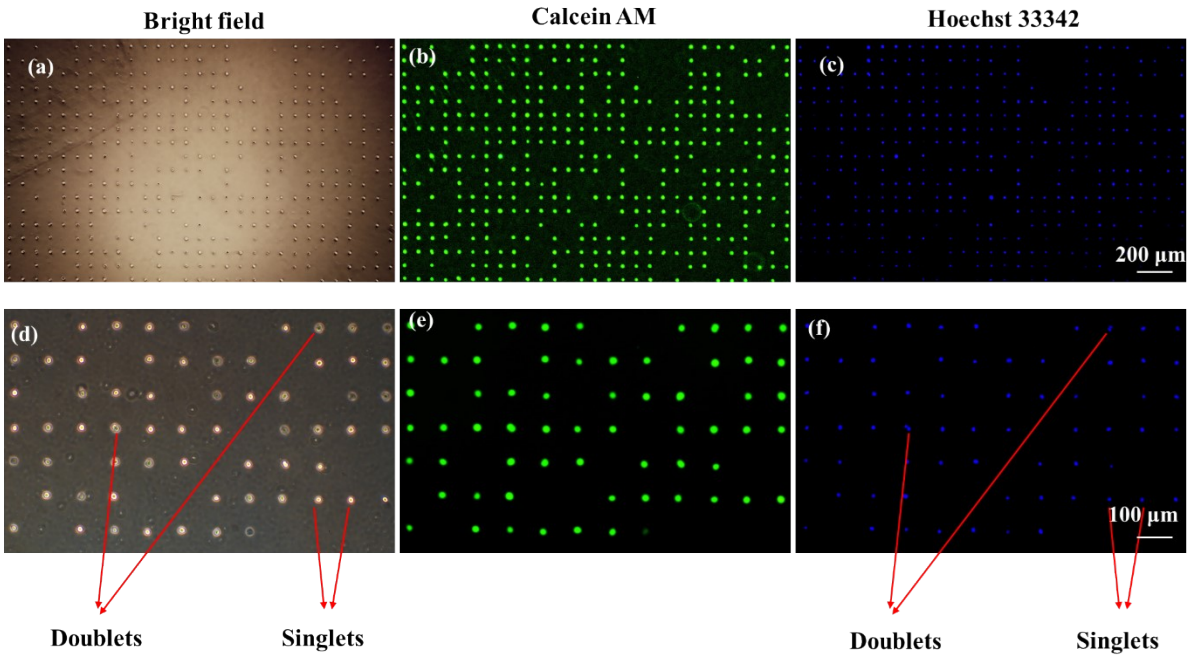

Figure S1: Bright field and fluorescent images showing clearly distinguishable cells. (a and d) show bright field images, (b and e) show viability staining (green channel), and (c and f) show nuclear staining (blue channel).

Synthesis and characterization of rGO nanoflakes

Graphene oxide (GO) was synthesized from graphite using the Tour (improved) method, an efficient approach for producing hydrophilic GO with high yield. In this process, graphite powder was oxidized using potassium permanganate in a mixed acidic medium of sulfuric and phosphoric acid under controlled stirring and temperature conditions. Sonication was employed to enhance intercalation, oxidation efficiency, and particle size reduction. After oxidation, the reaction mixture was diluted with deionized water, and hydrogen peroxide was then added to remove residual permanganate and manganese dioxide, yielding a bright yellow suspension. The product was allowed to settle and was repeatedly washed with hydrochloric acid, ethanol, and water until a neutral pH was achieved. The washed material was then dried to obtain GO powder. This method yielded more GO than conventional and modified Hummers' methods. Subsequently, GO was reduced to reduced graphene oxide (rGO) using a green reduction approach involving high-power ultraviolet irradiation, which removed most oxygen-containing functional groups, restored the graphitic structure, and enhanced rGO's photothermal properties.

The produced rGO was characterized using Raman spectroscopy, UV-Visible spectroscopy, FTIR, and TEM imaging. Raman spectrum and TEM images are showed in **Figure S2.**

Fabrication of micropatterned rGO device

The micropatterned rGO device (2 cm × 2 cm) was fabricated on a glass coverslip to generate arrays of circular rGO islands with diameters of 10 µm and 30 µm, respectively. The glass substrate was first thoroughly cleaned with piranha solution, then sequentially rinsed with

deionized water, acetone, and isopropanol, and finally dried under nitrogen. After prebaking to remove residual moisture, the coverslip was spin-coated with positive photoresist (AZ5214E), soft-baked, and patterned using UV photolithography with a designed photomask. The exposed photoresist was developed to create the desired micropattern. A graphene oxide (GO) solution was then drop-cast onto the patterned substrate and dried. Lift-off was performed by brief sonication in acetone, leaving behind an ordered array of circular GO micropatterns. Finally, the patterned GO regions were selectively reduced to reduced graphene oxide (rGO) by high-power UV irradiation. This process enabled the fabrication of uniform rGO island arrays with diameters of 10 μm and inter-island spacing of 30 μm, suitable for high-throughput cellular transfection applications. Fabrication steps and Images of fabricated device are shown in **Figure S2.**

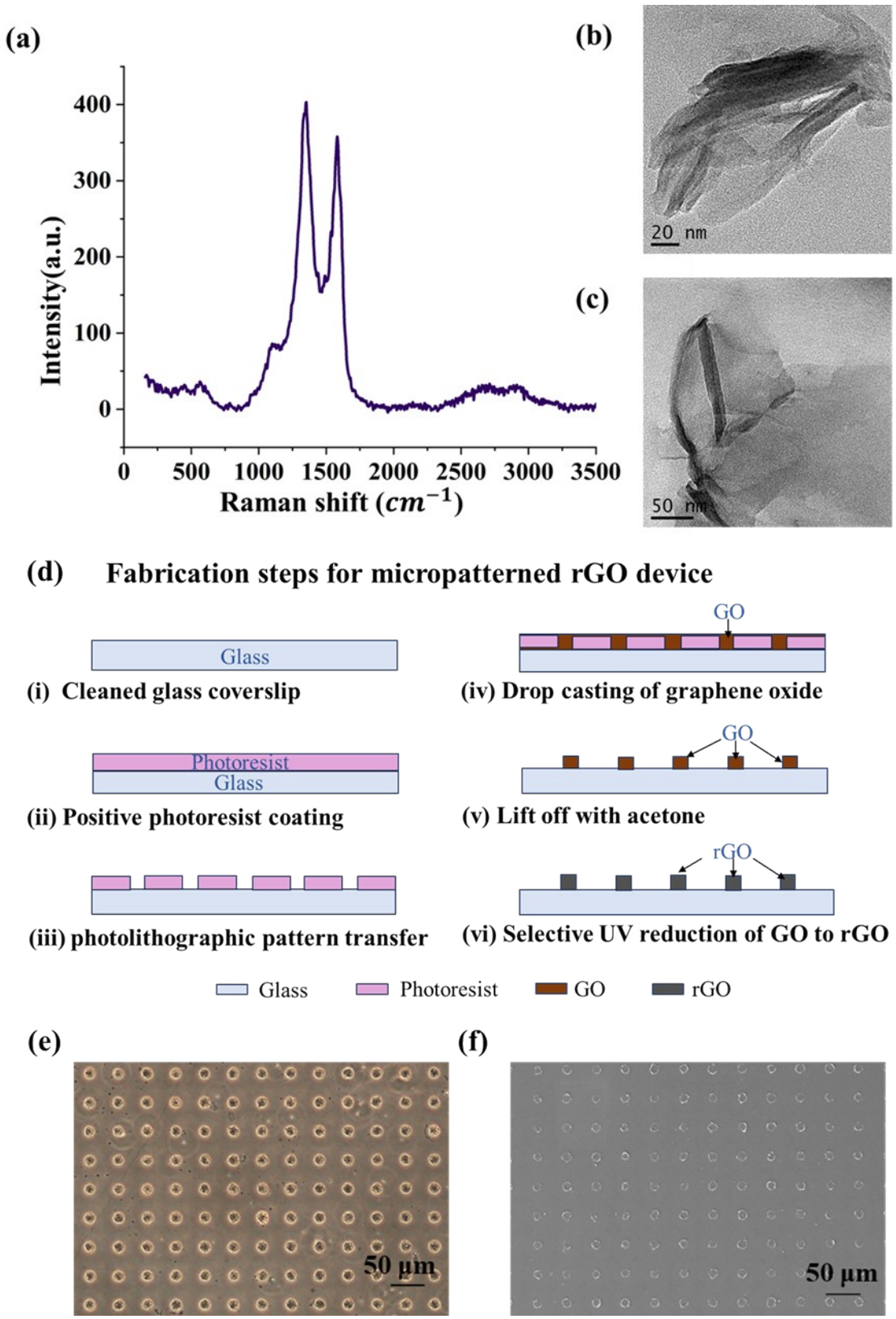

Figure S2.The rgo synthesis and micropatterned device fabrication. (a) Raman spectra of rGO nanoflakes with corresponding D band and G band. (b) and (c) show TEM images of rGO nanoflakes. (d) Illustration of fabrication steps involved in making the micropatterned rGO device, (e) Optical and (b) SEM image of the micropatterned rGO device.

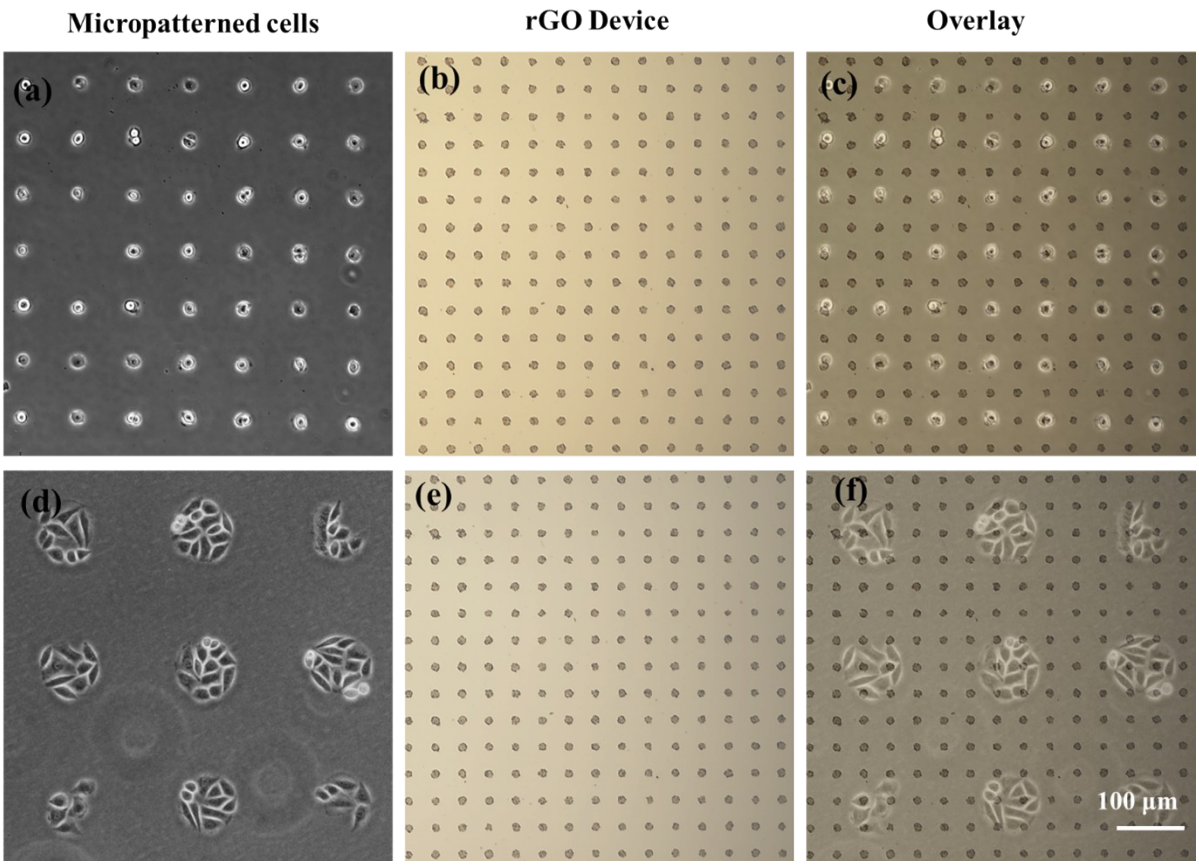

Figure S3: Images of the cellular micropatterns, micropatterned rGO device and overlay image showing alignment of rGO device over cells. (a and d) Micropatterned single cell array and cluster cell array (b and d) optical image of micropatterned rGO device and (c and f) overlay image of micropatterned cells and micropatterned rGO device.

Table S3: Effect of cargo size on photoporation parameters, showing the relationship between molecular size, required laser exposure (via scanning speed), delivery efficiency, and cell viability for L929 cells

Cargo Type	Approx. Size	Scanning Speed	Delivery Trend	Achieved delivery efficiency	Achieved cell viability
PI dye	~668 Da	15 mm/s	High efficiency at fast scanning	83.24%	91.20%
siRNA	~13 kDa	10 mm/s	Moderate exposure required	87.54%	95.10%
Plasmid DNA	~229 kDa	7 mm/s	Longer exposure needed	87.16%	92.59%
β-galactosidase	~465 kDa	5 mm/s	Longest exposure required	86.74%	89%

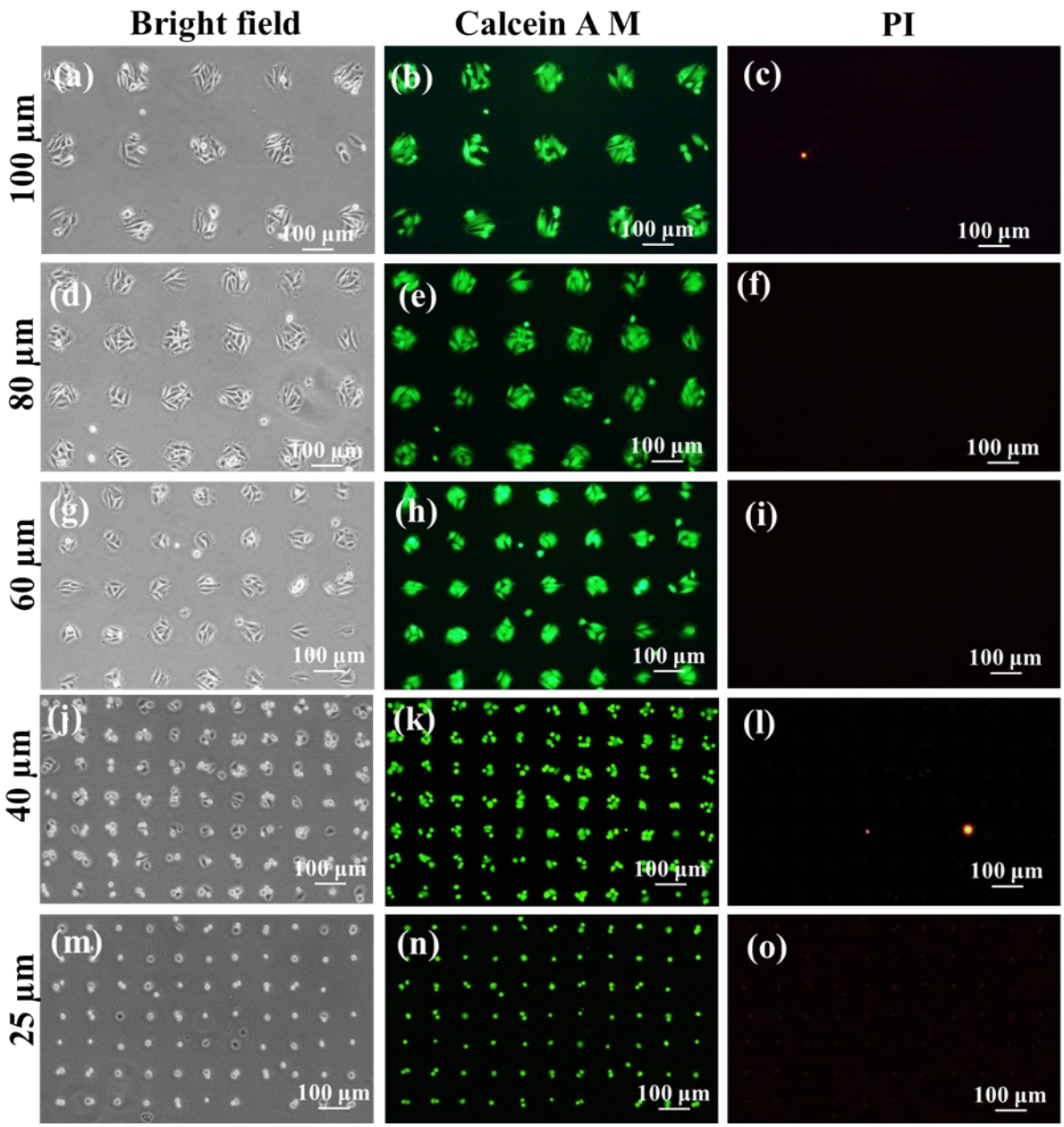

Figure S4. Bright field and fluorescence microscopy images showing live-dead staining with Calcein AM and PI dye performed in LN-229 cell patterning for through-hole dimensions of 100 µm (a, b, c), 80 µm (d, e, f), 60 µm (g, h, i), 40 µm (j, k, l), and 25 µm (m, n, o).

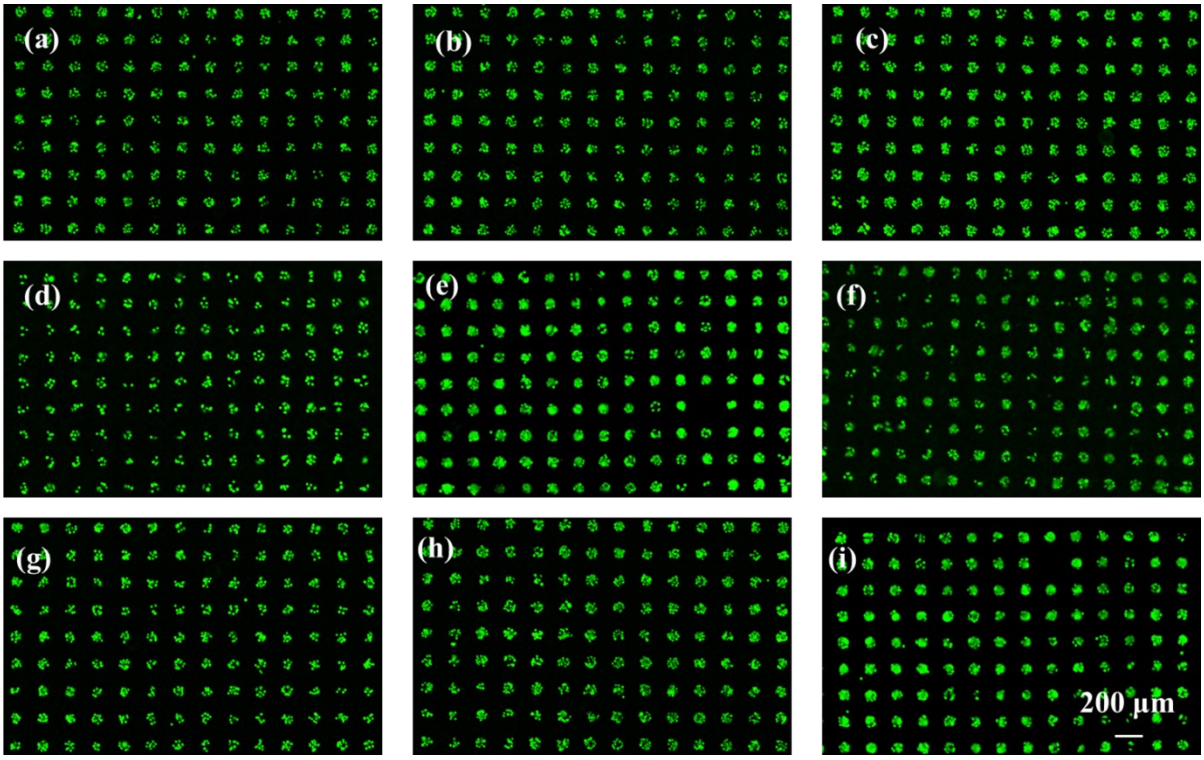

Figure S5: Low magnification(4X) Fluorescence images of cellular micropatterns (a-i) formed using a PDMS stencil membrane with microholes of 80 µm in diameter, showing a total of 1215 individual cell micropatterns.

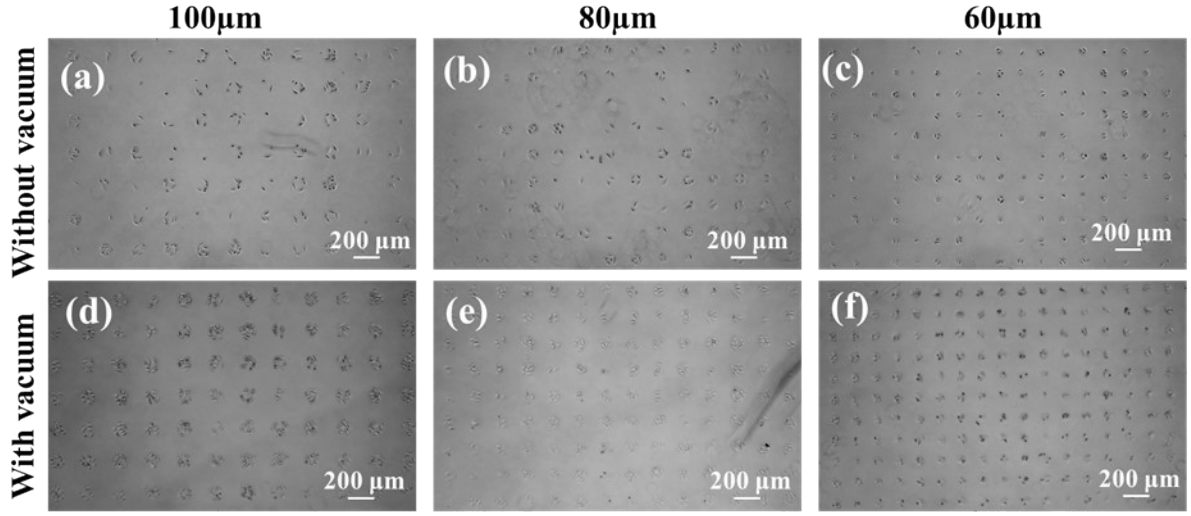

Figure S6. Bright field images displaying cell patterning across through-hole sizes of 100 µm (a and d), 80 µm (b and e), and 60 µm (c and f) for LN-229 cells, with and without a vacuuming step during cell seeding. The images clearly demonstrate how the vacuuming step enhances

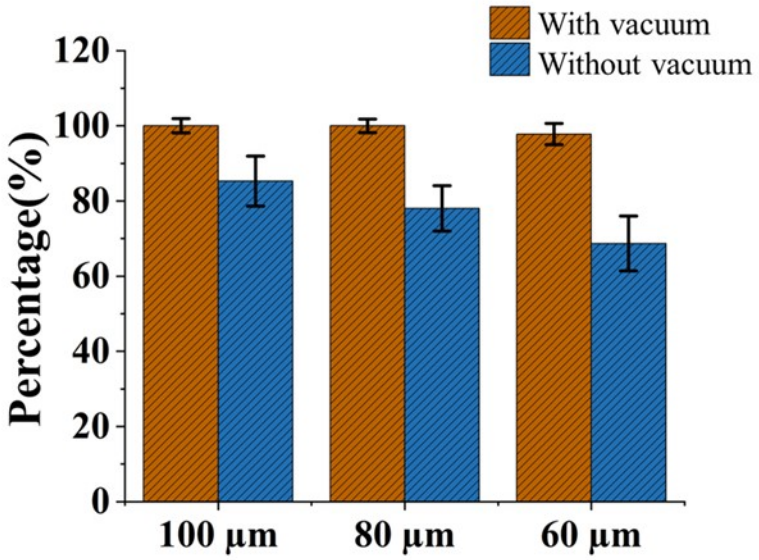

patterning efficiency.

Figure S7. The graphical plot illustrates differences in patterning efficiency during cell micropatterning in LN-229 cells across through-hole dimensions of 100 µm, 80 µm, and 60 µm, with and without a vacuuming step prior to cell seeding.

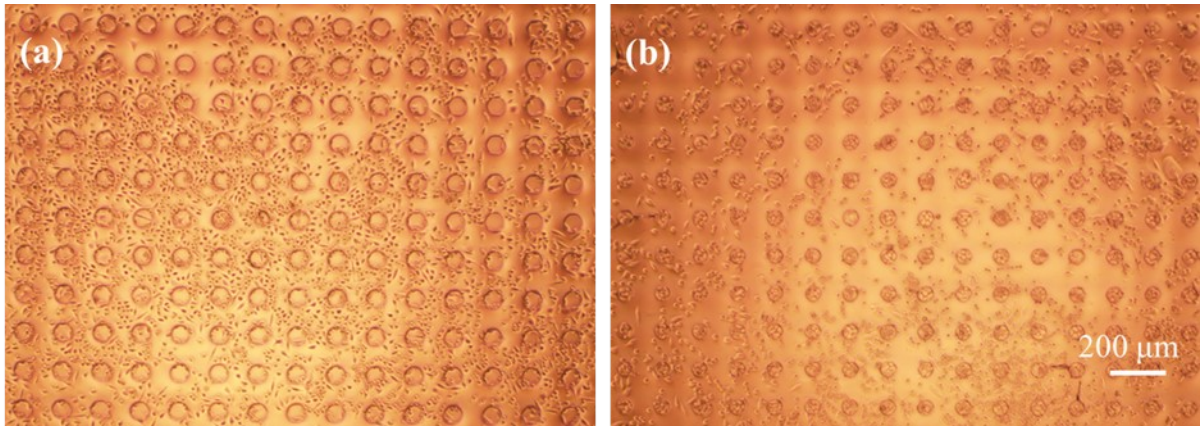

Figure S8. Bright field images displaying SiHa cell trapping across the through-hole diameter of 60 µm (a) without and (b)with a vacuuming step before cell seeding. The images clearly demonstrate that the vacuuming step increases the cell-trapping capability.

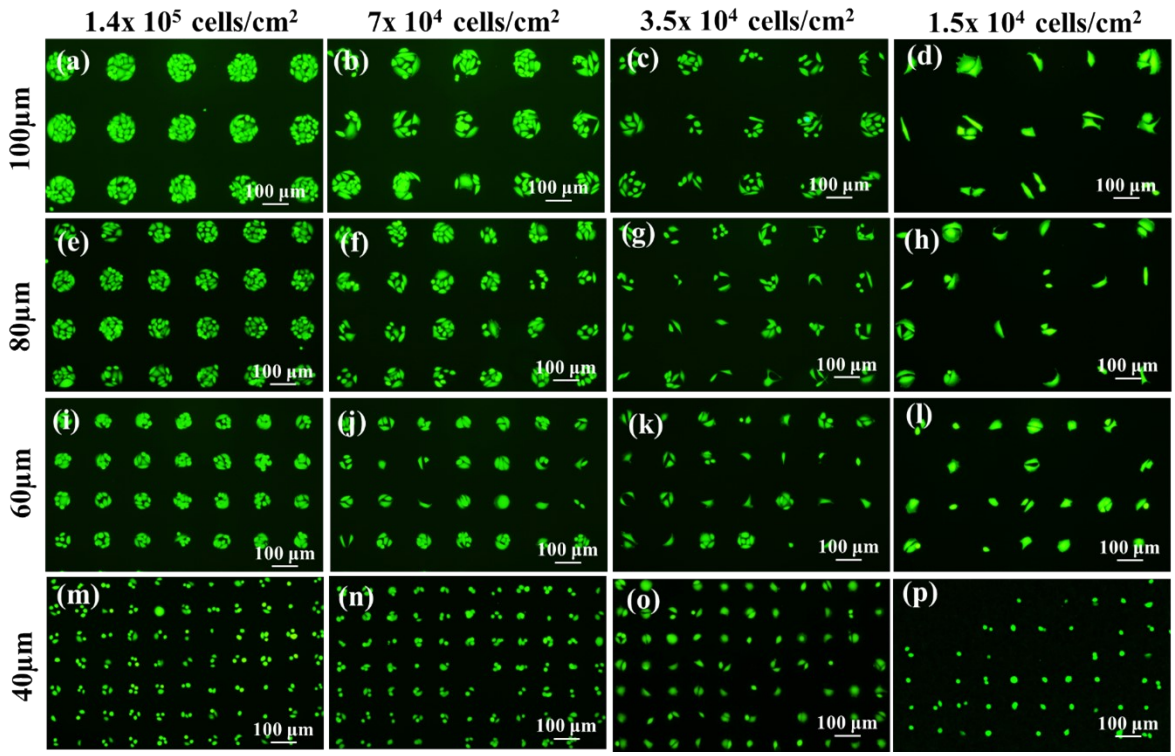

Figure S9. Fluorescence microscopy images showing cell patterning across through-hole dimensions of 100 µm (a, b, c, and d), 80 µm (e, f, g, and h), 60 µm (i, j, k, and l), and 40 µm (m, n, o, and p) at different cell seeding concentrations for SiHa cells

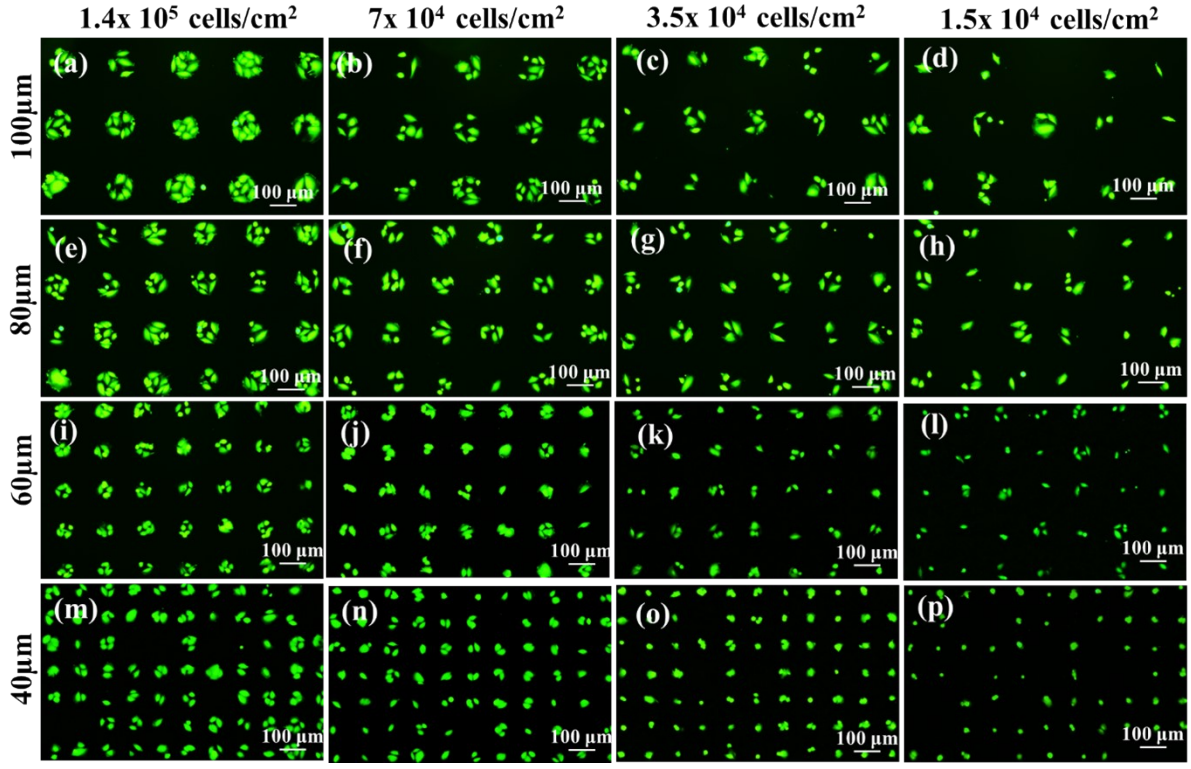

Figure.S10. Fluorescence microscopy images showing L929 cell patterning for across

through-hole dimensions of 100 µm (a,b,c, and d), 80 µm (e,f,g, and h), 60 µm (i,j,k, and l), and 40 µm (m,n,o, and p) at varying cell seeding concentrations for L929 cells.

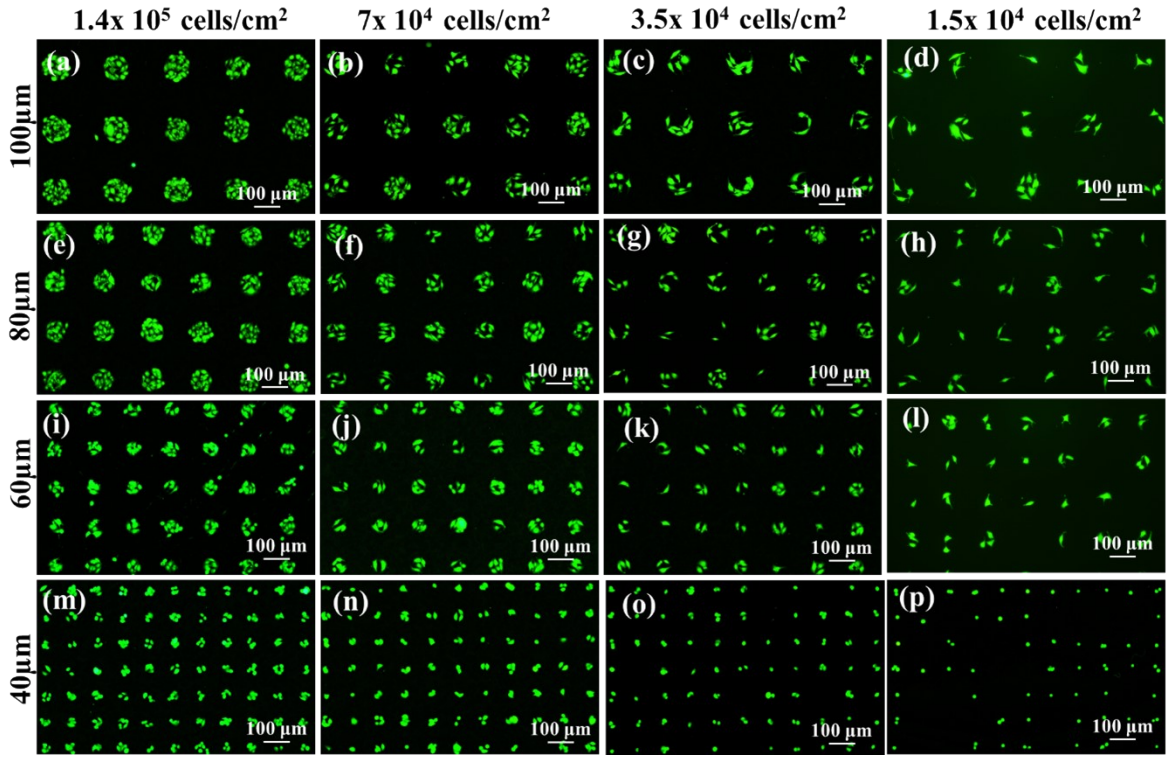

Figure S11. Fluorescence microscopy images showing cell patterning across through-hole dimensions of 100 µm (a,b,c, and d), 80 µm (e,f,g, and h), 60 µm (i,j,k, and l), and 40 µm (m,n,o, and p) at different cell seeding concentrations for LN229 cells.

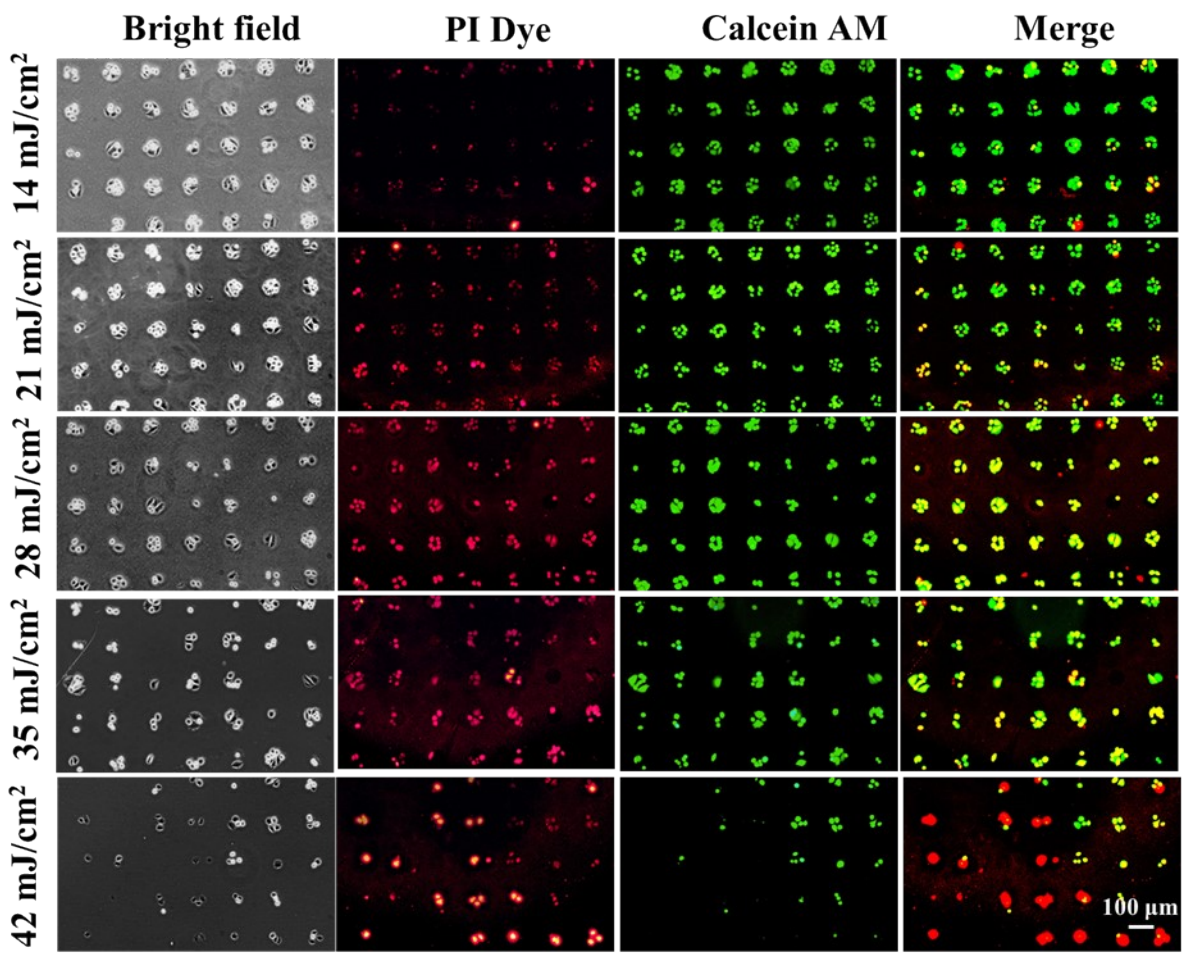

Figure S12. Optimization of laser fluence. Image shows brightfield and corresponding fluorescence images of the SiHa cell micropatterns (60 µm diameter) which underwent PI delivery under varied laser fluence with scanning speed kept constant at 15mm/s.

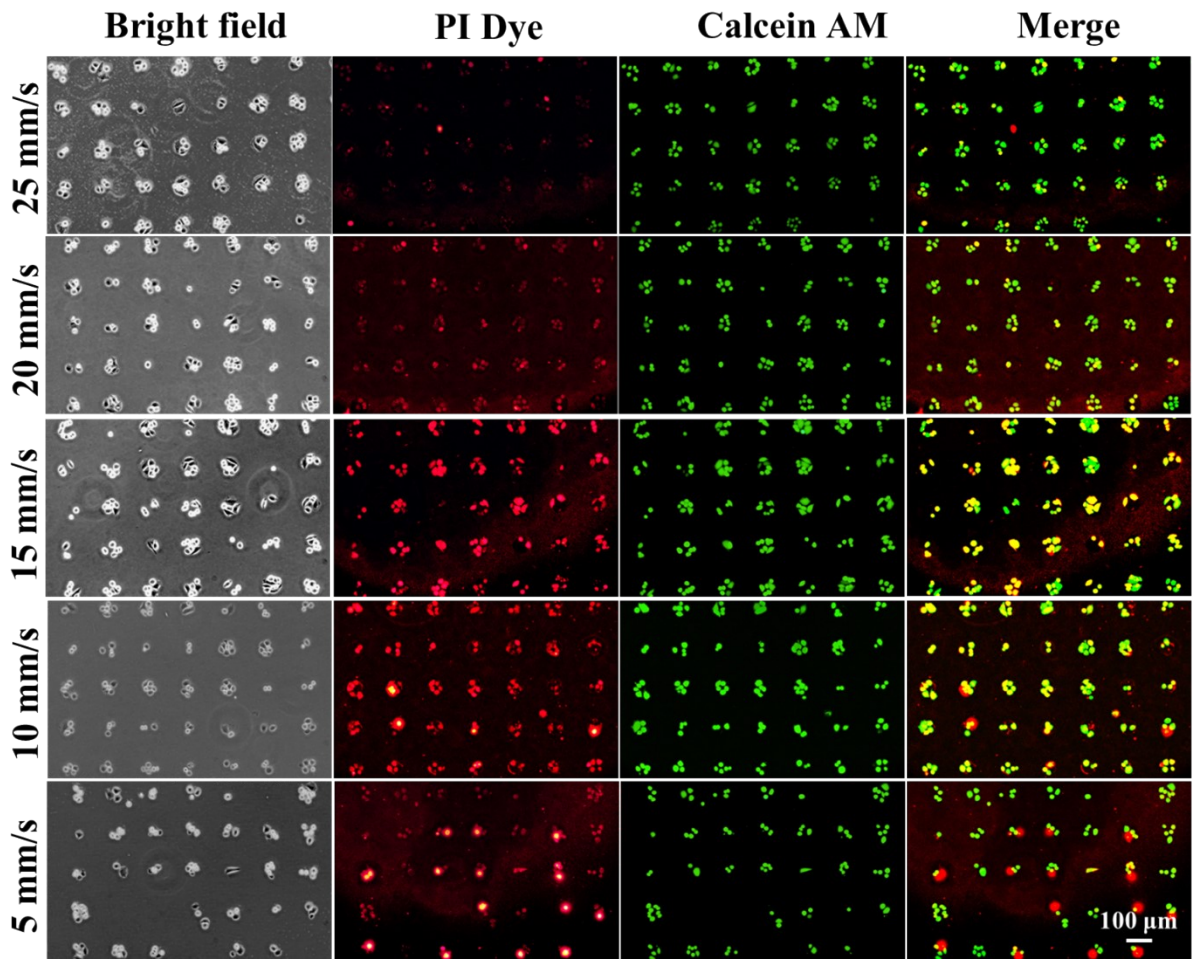

Figure S13. Optimization of laser scanning speed. Image shows brightfield and corresponding fluorescence images of the SiHa cell micropatterns (60 µm diameter) which underwent PI delivery under varied laser scanning speed with fluence kept constant at 28 mJ/cm^2.

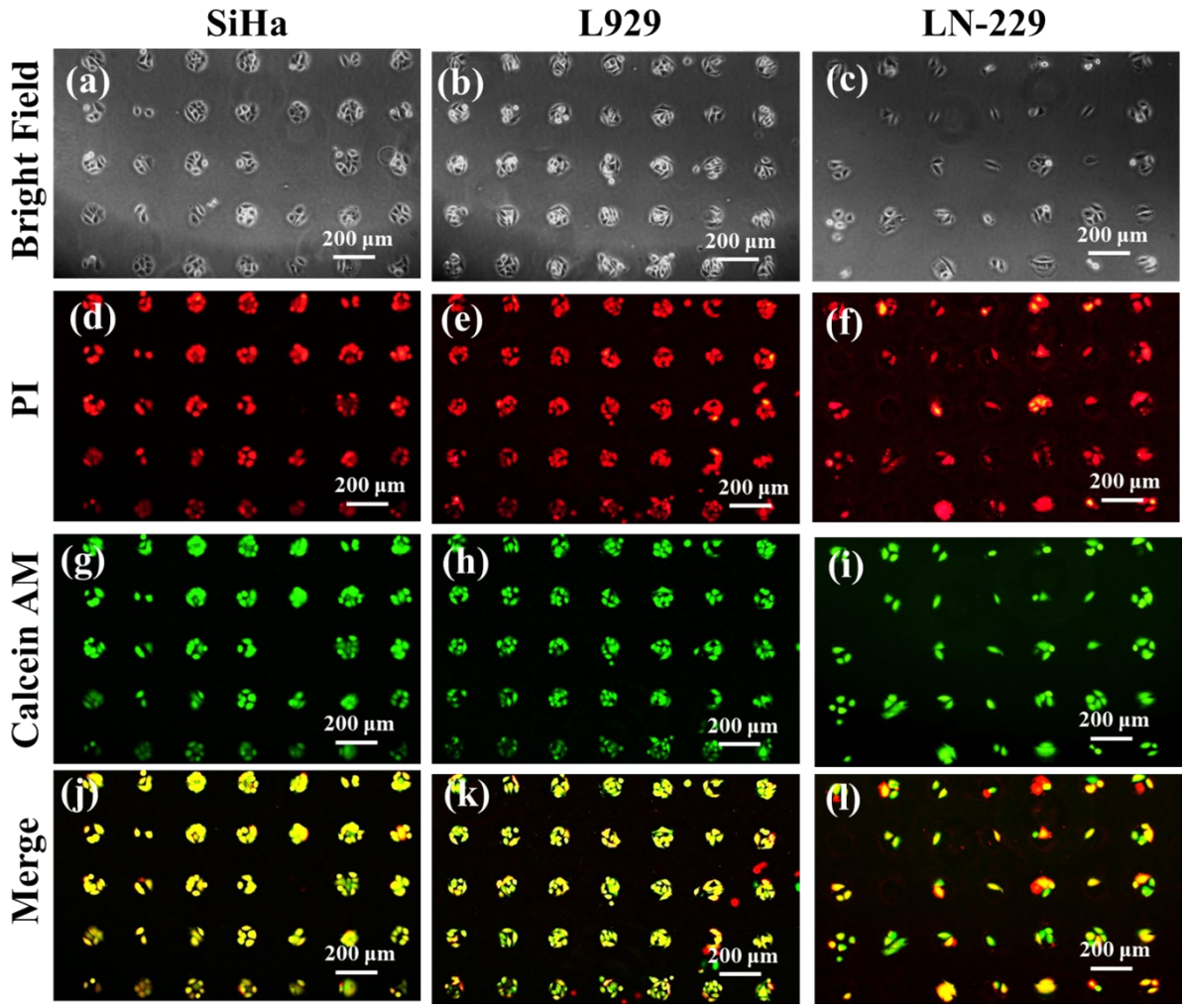

Figure S14. Intracellular delivery of PI dye in micropatterned cells using the micro-patterned rGO device. Brightfield images (a–c) and corresponding fluorescence images (red) (d–f) demonstrate PI dye delivery in SiHa, L929, and LN-229 cells. Cell viability assessment is shown in green fluorescence images (g–i), while merged images (j–l) display green to yellowish-green signals, confirming the presence of viable cells following PI dye delivery in micropatterns generated with a 60 µm through-hole PDMS stencil.

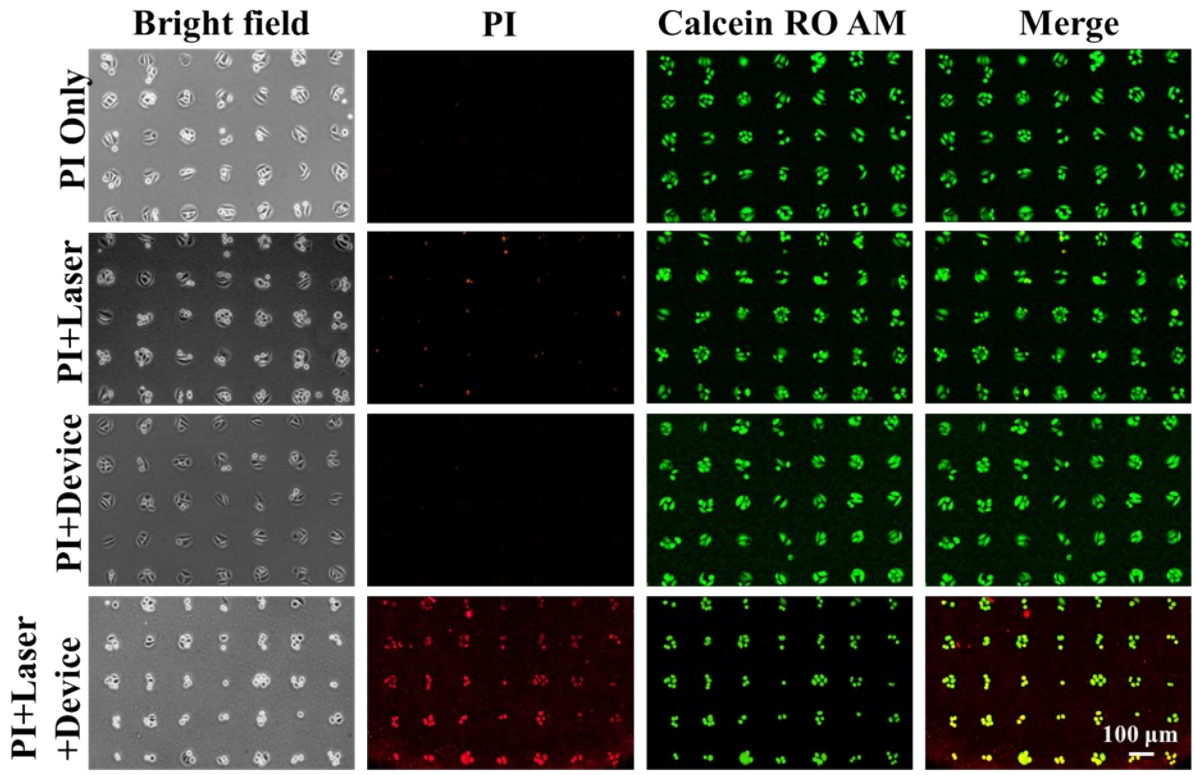

Figure S15. Control experiment showing the requirement of rGO device for intracellular delivery of plasmid for PI delivery at optimized laser parameters(1064 nm,15 mm/s, and 28 mJ/cm^2). Bright field and fluorescence images of SiHa cells incubated with PI but neither exposed to a laser nor to rGO device, SiHa cells incubated with PI and exposed to a laser without rGO device, images of SiHa cells incubated with PI exposed to the rGO device but not to a laser and images of SiHa cells incubated with PI exposed to the rGO device in the presence of laser. Red fluorescence in PI images indicates the delivered cells, while the green fluorescence in Calcein images indicates viable cells. In the merged image, the yellow to greenish-yellow colour of cells indicates delivered cells that are live, the red colour indicates dead cells after delivery, and the green colour indicates live and undelivered cells.

Table S4. Quantitative comparison for delivery efficiency and cell viability for different control conditions.

Condition	**Delivery Efficiency**	**Cell Viability**
PI	~0%	~100%
(Device+PI)	~0%	~100%
(Laser+PI)	Low (~10%)	High (~99%-100%)
(Laser+Device+PI)	High (~72-84%)	High (~84–92%)

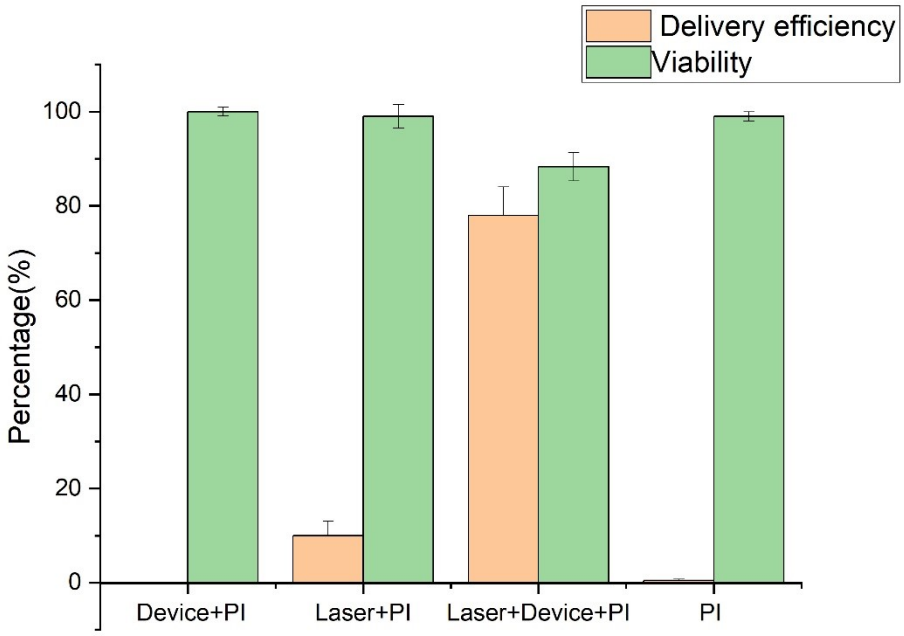

Figure S16: Graphical plot showing average delivery efficiency and cell viability obtained across different control experiment conditions

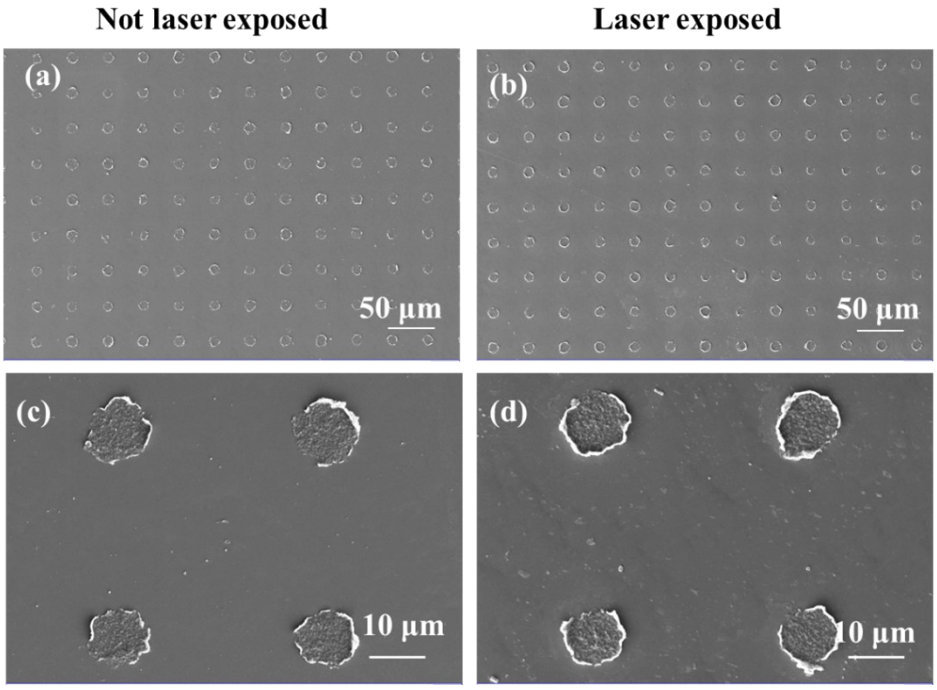

Figure S17: SEM images of the micropatterned rGO device (a,c) before and (b,d) after three cycles of laser exposure.

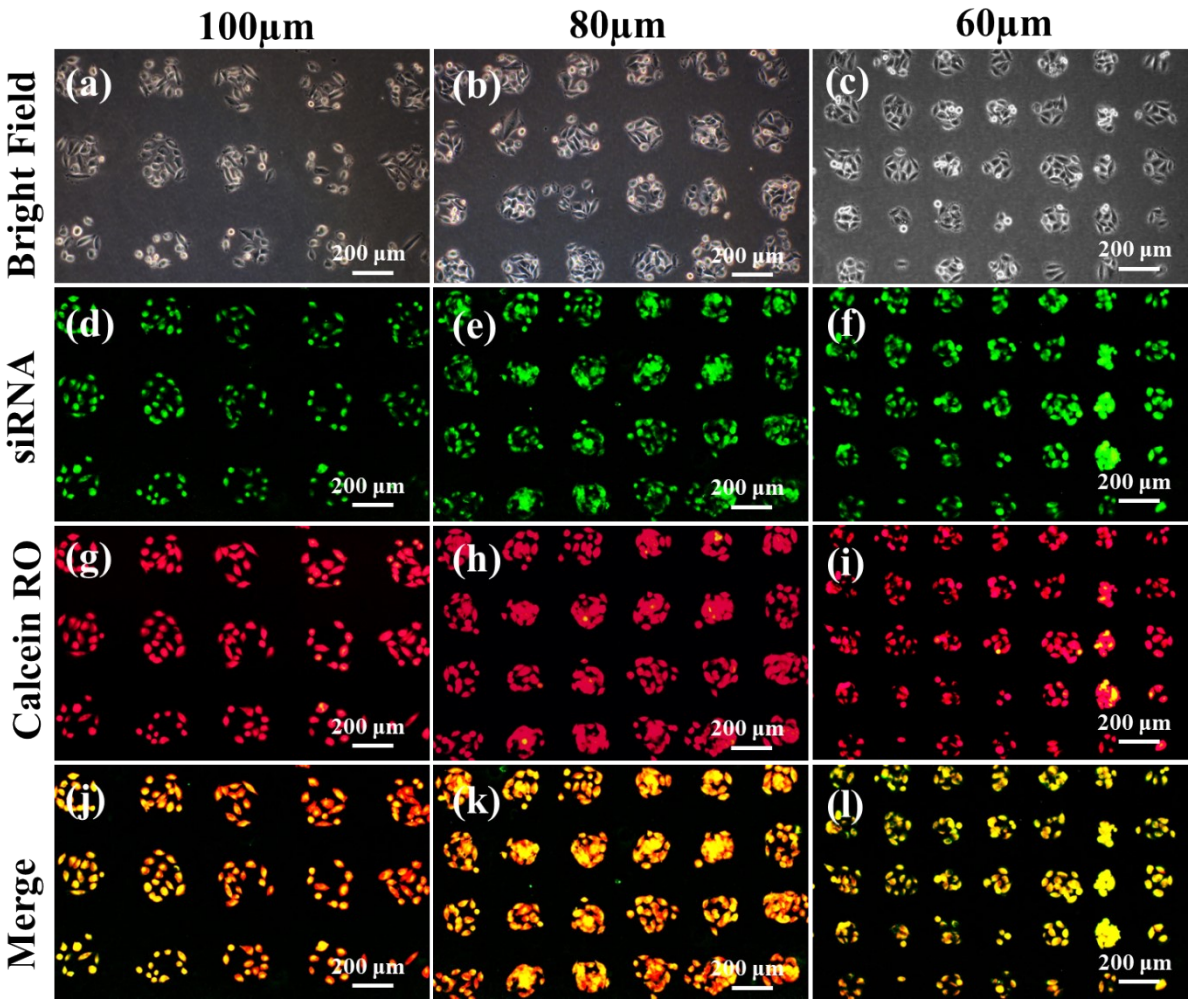

Figure S18. Transfection of siRNA in micropatterned cells using the micro-patterned rGO device. Brightfield images (a–c) and corresponding fluorescence images (green) (d–f) demonstrate siRNA transfection in LN229 cells. Cell viability assessment is shown in red fluorescence images (g–i), while merged images (j–l) display green to yellowish-green signals, confirming the presence of viable cells following siRNA transfection in micropatterns generated with 100 µm, 80 µm 60 µm through-hole PDMS stencils

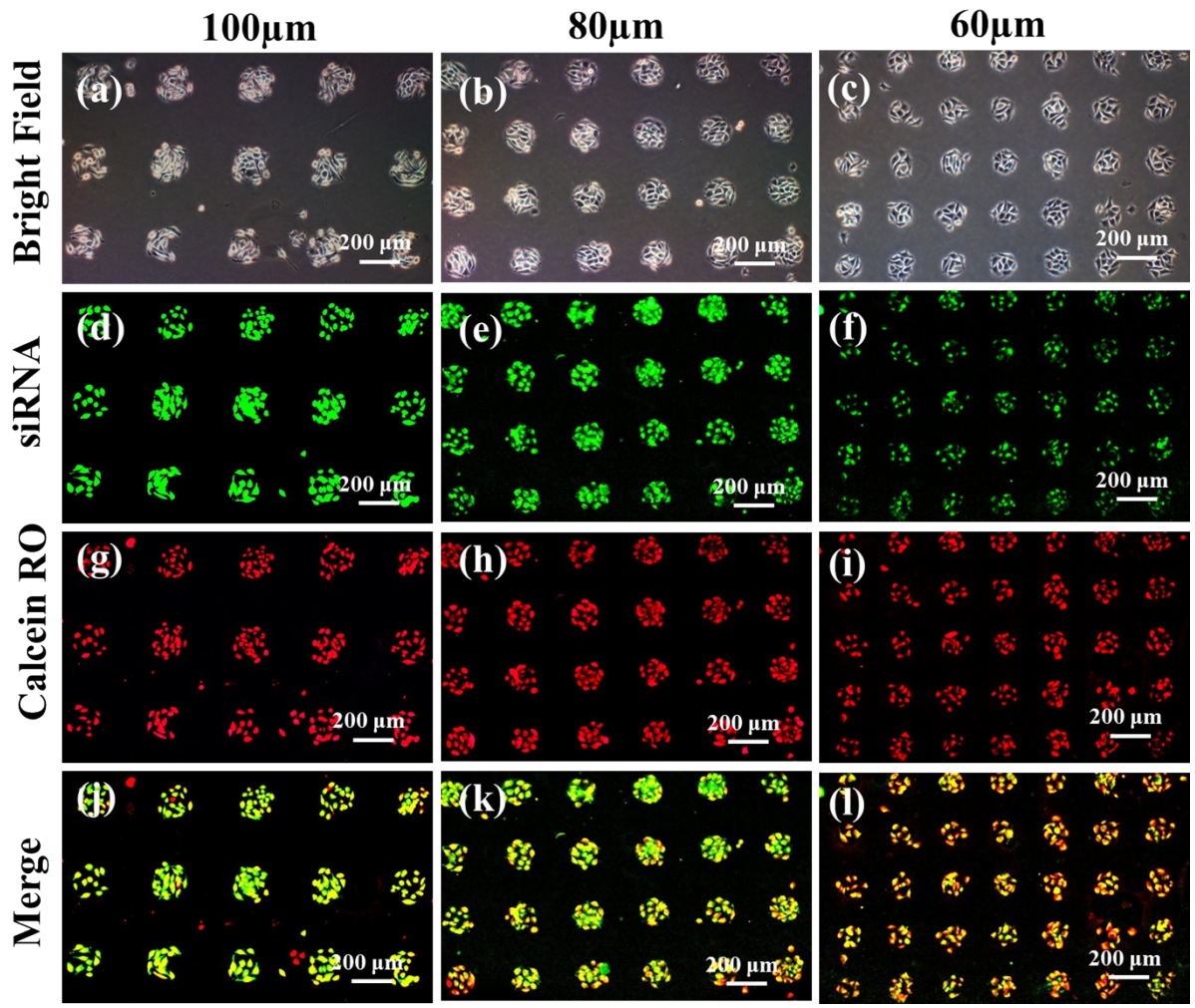

Figure S19. Transfection of siRNA in micropatterned cells using the micro-patterned rGO device. Brightfield images (a–c) and corresponding fluorescence images (green) (d–f) demonstrate siRNA transfection in L929 cells. Cell viability assessment is shown in red fluorescence images (g–i), while merged images (j–l) display green to yellowish-green signals, confirming the presence of viable cells following siRNA transfection in micropatterns generated with 100 µm, 80 µm 60 µm through-hole PDMS stencils

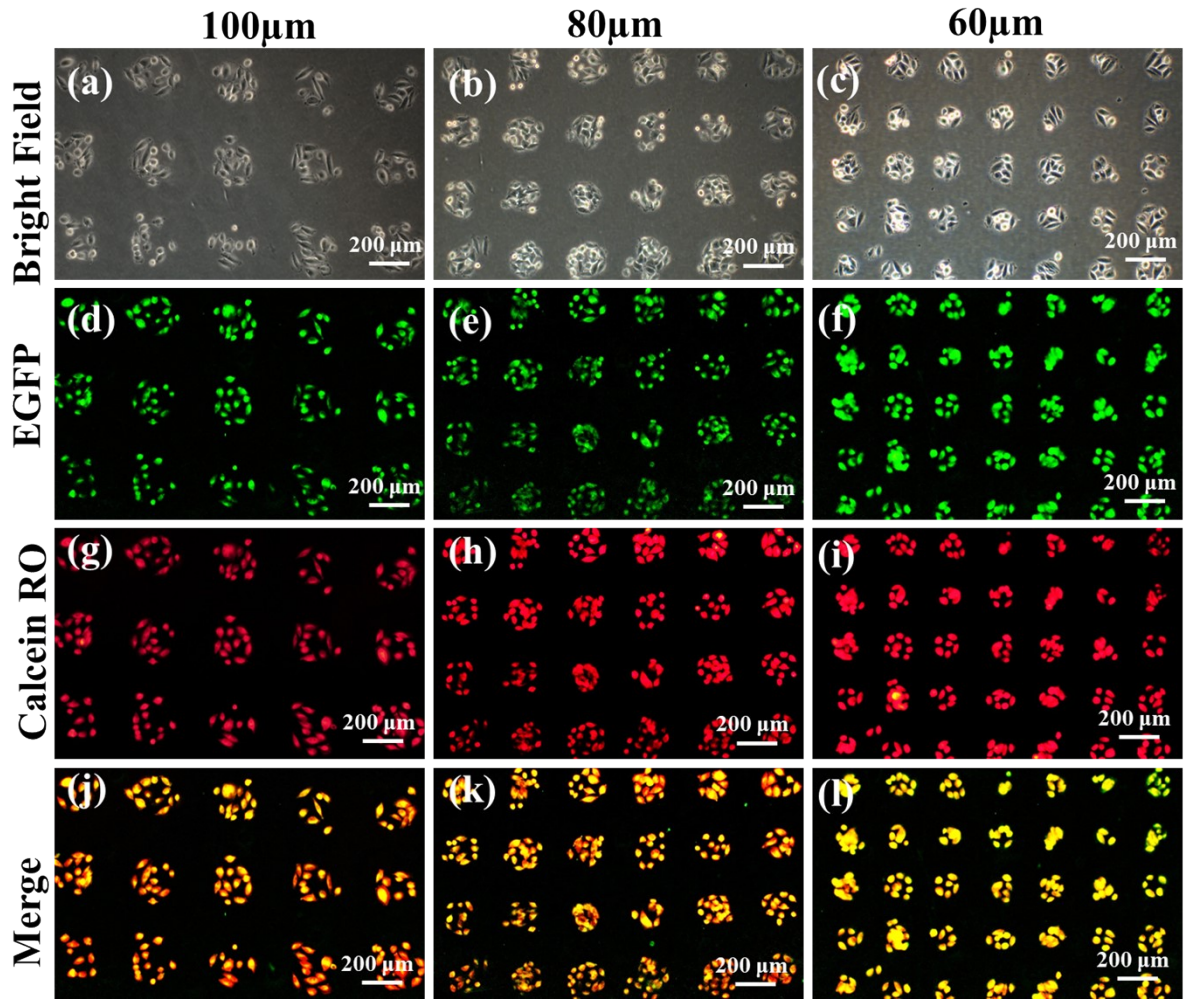

Figure S20. Transfection of EGFP in micropatterned cells using the micro-patterned rGO device. Brightfield images (a–c) and corresponding fluorescence images (green) (d–f) demonstrate EGFP transfection in LN229 cells. Cell viability assessment is shown in red fluorescence images (g–i), while merged images (j–l) display green to yellowish-green signals, confirming the presence of viable cells following EGFP transfection in micropatterns generated with 100 µm, 80 µm 60 µm through-hole PDMS stencils

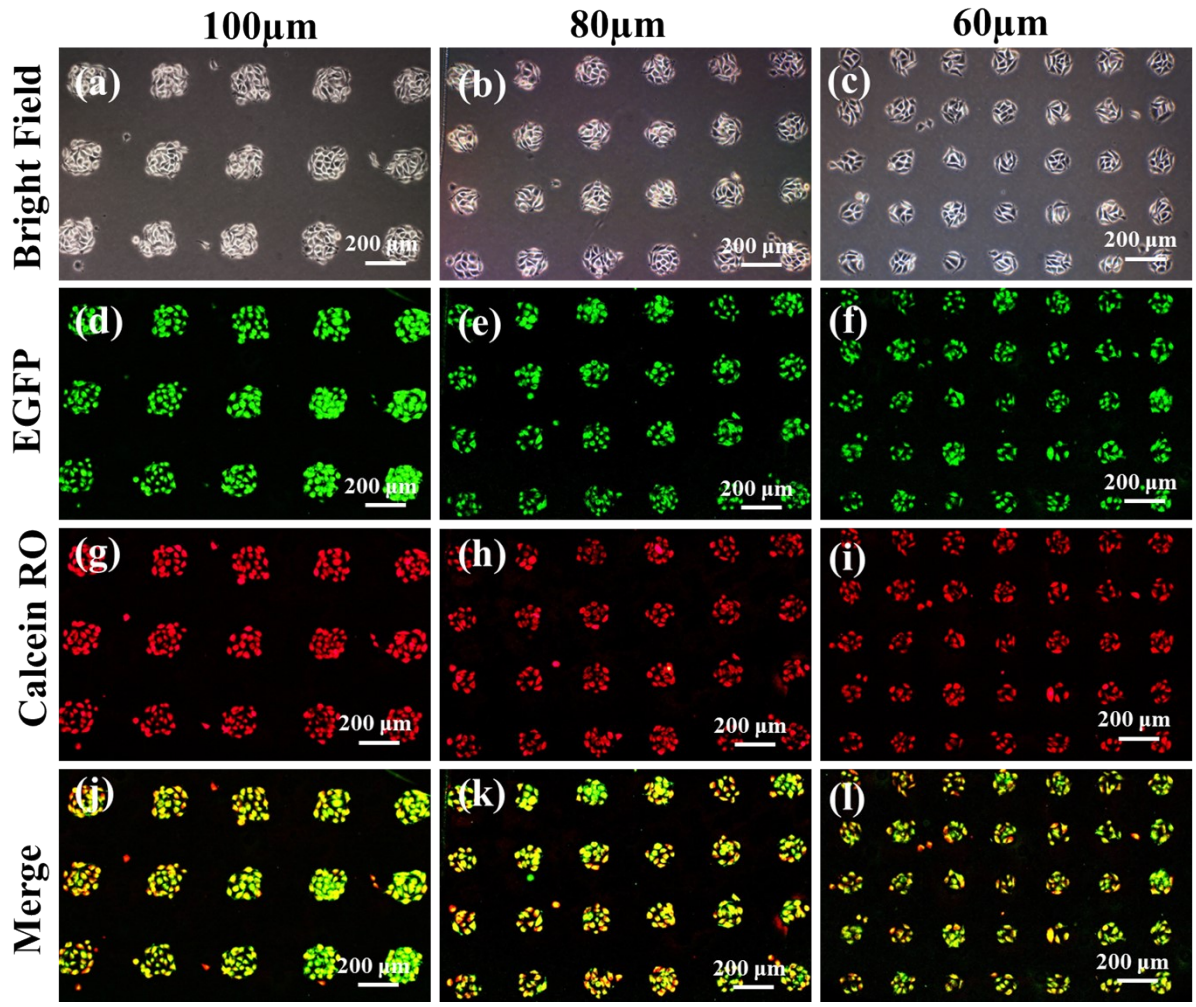

Figure S21. Transfection of EGFP in micropatterned cells using the micro-patterned rGO device. Brightfield images (a–c) and corresponding fluorescence images (green) (d–f) demonstrate EGFP transfection in L929 cells. Cell viability assessment is shown in red fluorescence images (g–i), while merged images (j–l) display green to yellowish-green signals, confirming the presence of viable cells following EGFP transfection in micropatterns generated with 100 µm, 80 µm 60 µm through-hole PDMS stencils

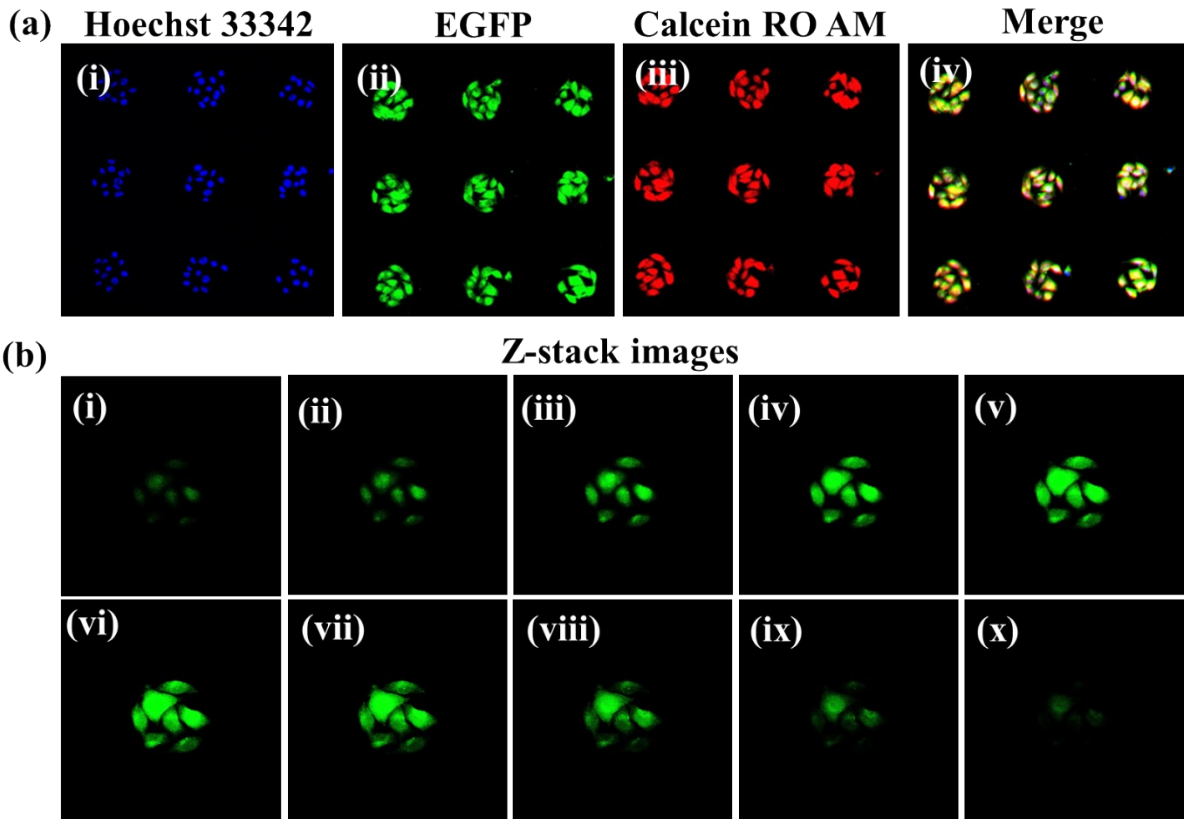

Figure S22. Confocal microscopy of EGFP delivery in L929 cells using 60 µm stencil patterns.(a) Representative array image shows uniform cellular patterning and uptake of siRNA across the patterned region. (c) Z-stack reconstruction confirms the intracellular distribution of

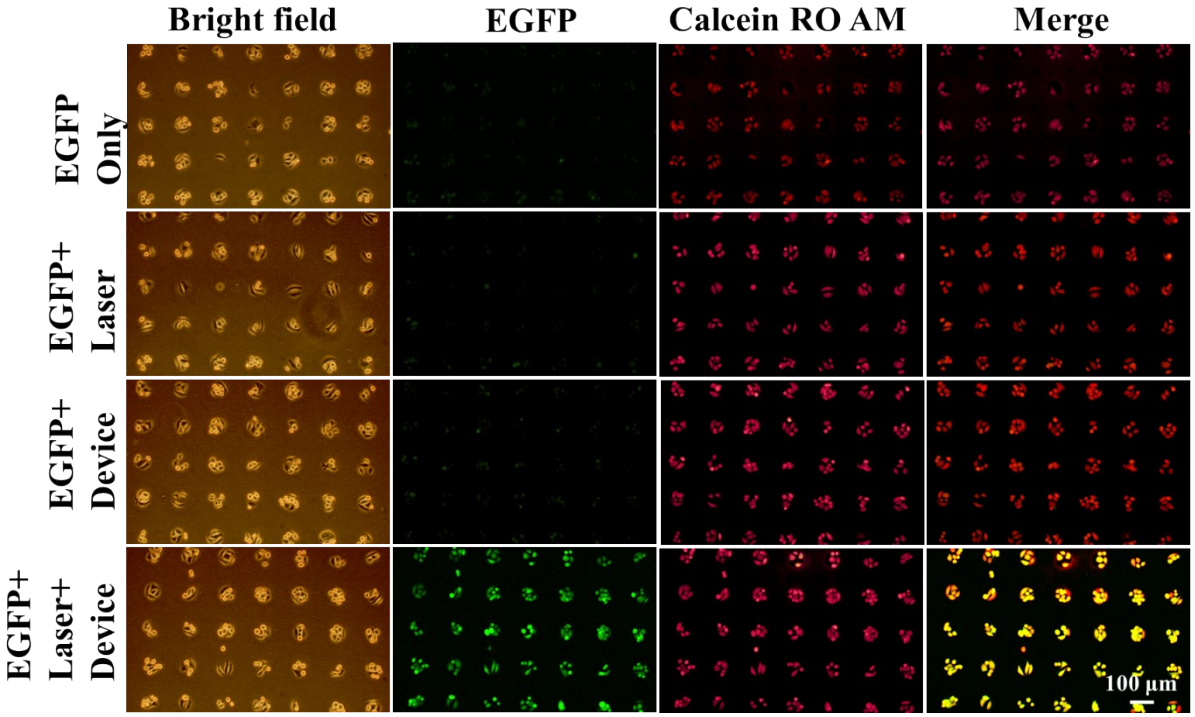

the delivered EGFP throughout the cell volume in a single pattern

Figure S23. Control experiment showing the requirement of rGO device for intracellular delivery of plasmid for EGFP expression at optimized laser parameters(1064 nm,7 mm/s, and 28 mJ/cm^2). Bright field and fluorescence images of SiHa cells incubated with EGFP but neither exposed to a laser nor to the rGO device, SiHa cells incubated with EGFP and exposed to a laser with and without the rGO device, and images of SiHa cells incubated with EGFP exposed to the rGO device but not to a laser and images of SiHa cells incubated with EGFP exposed to the rGO device in the presence of laser. Green fluorescence in EGFP images indicates delivered cells, while red-orange fluorescence in Calcein images indicates viable cells. In the merged image, the yellow-to-orange-yellow colour of cells indicates delivered cells that are live; green indicates dead cells after delivery; and red indicates live, undelivered cells.

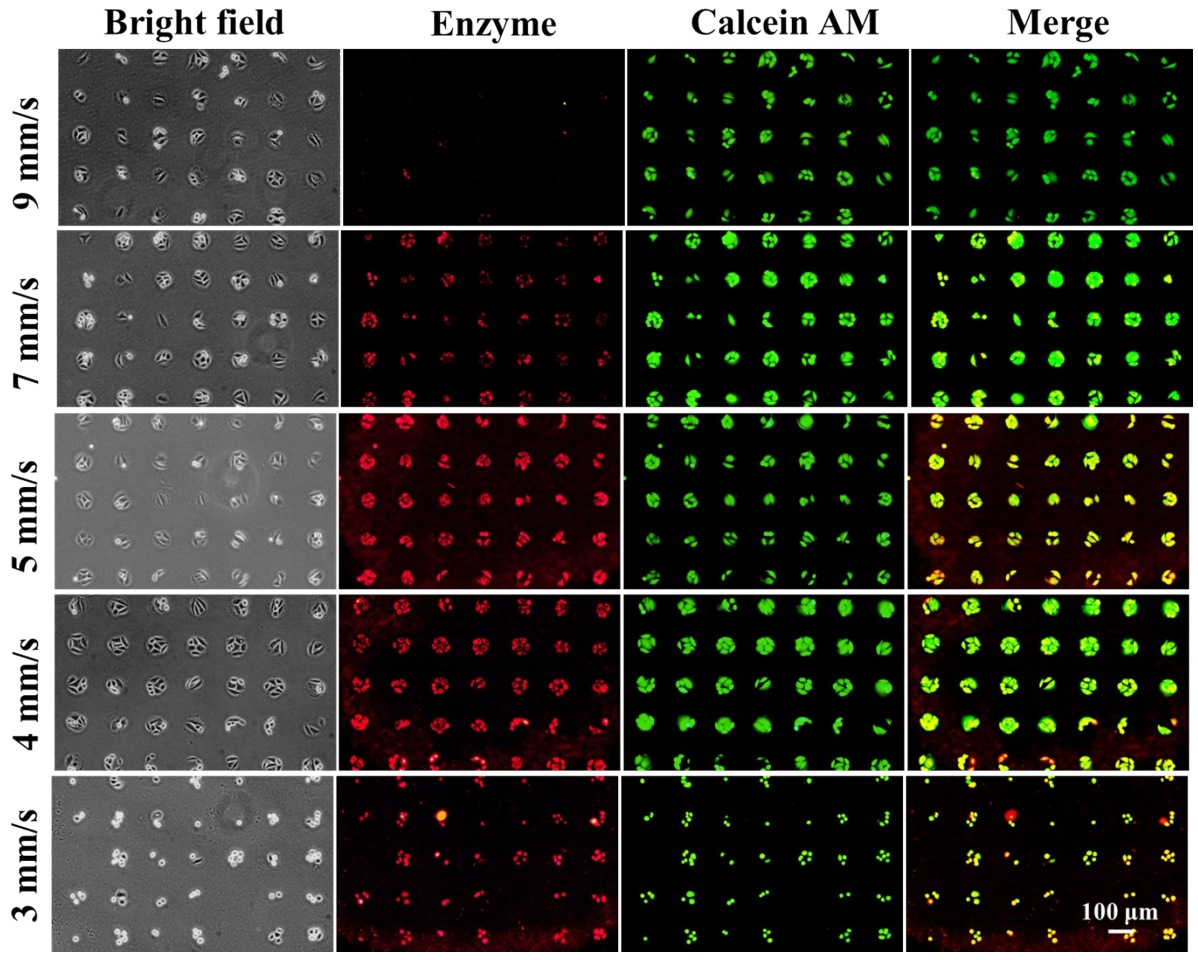

Figure S24. Optimization of laser scanning speed. Image shows brightfield and corresponding fluorescence images of the SiHa cell micropatterns (60 µm diameter) which underwent enzyme transfection under varied laser scanning speed with fluence kept constant at 28 mJ/cm^2.

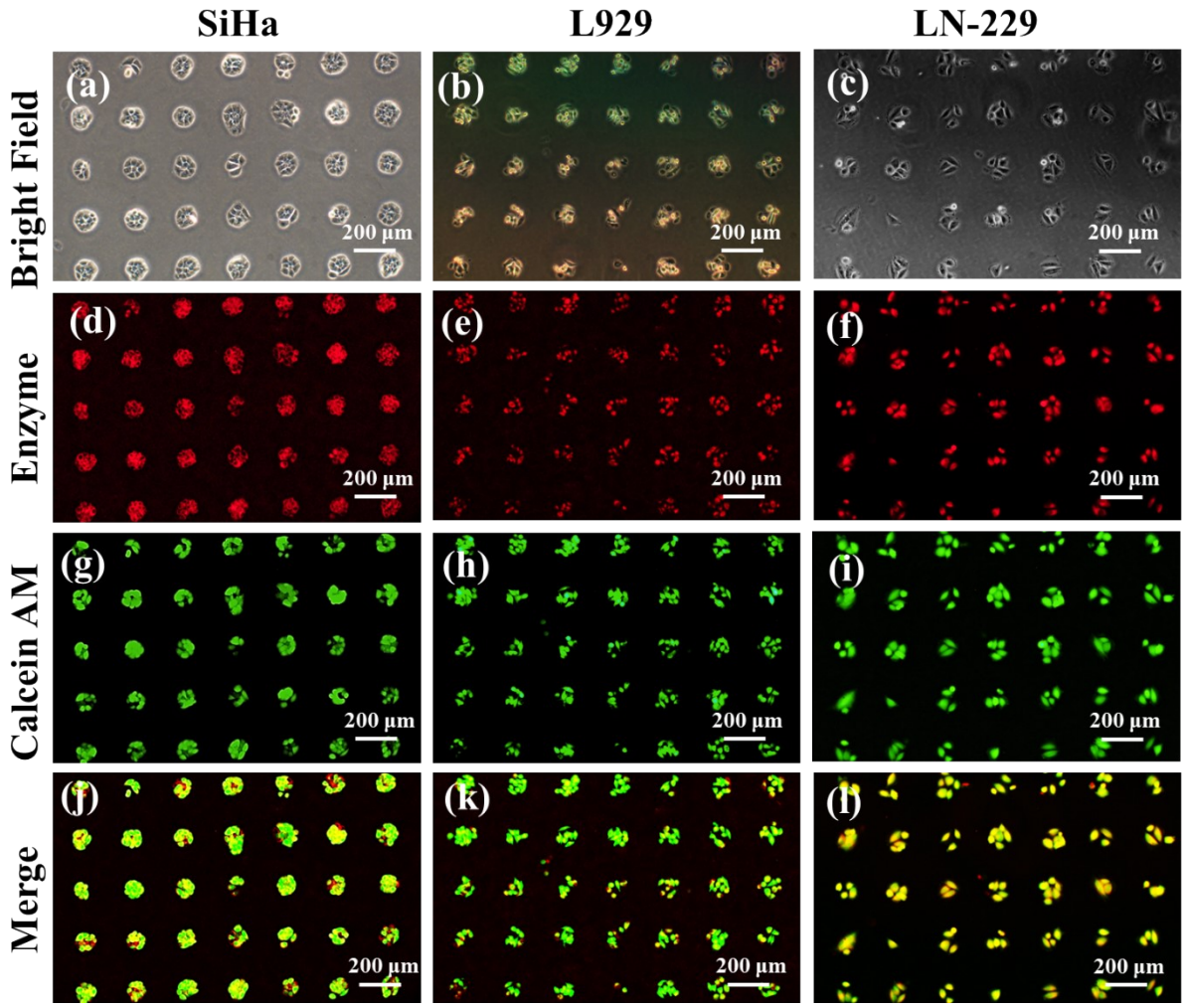

Figure S25. Transfection of β-galactosidase enzyme in micropatterned cells using the micro-patterned rGO device. Brightfield images (a–c) and corresponding fluorescence images (red) (d–f) demonstrate enzyme transfection in SiHa, L929, and LN-229 cells. Cell viability assessment is shown in green fluorescence images (g–i), while merged images (j–l) display green to yellowish-green signals, confirming the presence of viable cells following PI dye delivery in micropatterns generated with a 60 µm through-hole PDMS stencil

β-galactosidase activity assay

In addition to demonstrating intracellular uptake of Cy5-labeled β-galactosidase, we have also performed a β-galactosidase activity assay to evaluate whether enzymatic function is preserved following post-delivery. After 24 h of β-galactosidase transfection, the cells were incubated with β-galactosidase assay reagent under standard cell culture conditions for 30 min. Subsequently, β-galactosidase assay stop solution was added to terminate the reaction. The enzymatic activity of β-galactosidase was then quantified by measuring the absorbance at 405 nm.

The results (**Figure S26)** showing increased enzymatic activity in sample when compared with the control confirm that the delivered protein retains its enzymatic activity inside the cells, indicating that the photoporation process does not significantly compromise protein functionality under the applied conditions. These findings demonstrate that our platform enables not only the delivery of large biomolecules (~465 kDa), but also the preservation of their biological activity post-delivery.

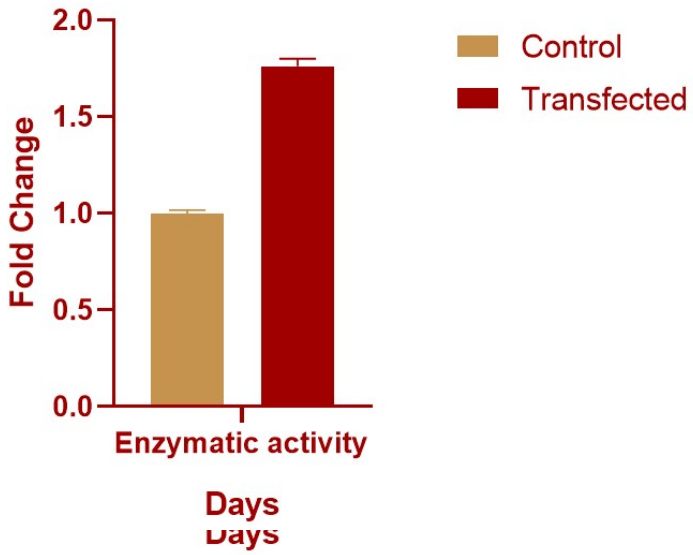

Figure S26: Graph quantifying the fold change of β-Galactosidase enzymatic activity in control and the β-gal enzyme-transfected cells.

Assessment of the cytocompatibility of the platform

To evaluate the potential impact of our platform on cellular health beyond short-term viability, we performed additional studies, including (i) a 3-day proliferation assay (MTT) (**Figure S27**) and (ii) DNA fragmentation analysis (**Figure S28**) performed on cells exposed to the photoporation conditions. For MTT assay we had one control and three samples. control consisted of hMSCs (human mesenchymal stem cells) that were neither subjected to laser exposure nor exposed to the rGO device (Control), samples consisted of cells that were subjected to laser exposure without the micro-patterned rGO device (Laser), cells exposed to rGO device with no laser exposure (Device), and cells that were subjected to laser exposure with the micro-patterned rGO device aligned on top of cells (Device+Laser). Data represent mean ± SD (n = 3). MTT assay results (mean ± SD, n = 3) show a progressive increase in (absorbance) metabolic activity from Day 1 to Day 3 across all groups. The results indicate sustained metabolic activity.

Next, we performed a DNA fragmentation assay(HCS DNA Kit) to detect apoptosis by checking for DNA fragmentation during photoporation using our platform. During apoptosis DNA breaks into fragments and the kit labels this DNA break using fluorescent markers. We used HCS DNA damage kit for this assay. It uses Anti-γH2AX antibody and Fluorescent secondary antibody (Alexa Fluor 555), giving bright red fluorescence to DNA fragments.

Figure S28 shows results of DNA fragmentation assay; the absence of red signal (**Figure S28c** and **S28g**) indicates that neither the control nor the sample has got fragmented DNA. Bright green signal from Calcein AM(**Figure S28b** and **S28f**) and Hoechst(**Figure S28a** and **S28e**) confirms the viability of the cells, both in control and sample.

Combined, results suggest minimal long-term cytotoxicity and absence of apoptosis induced by the photoporation process using our platform.

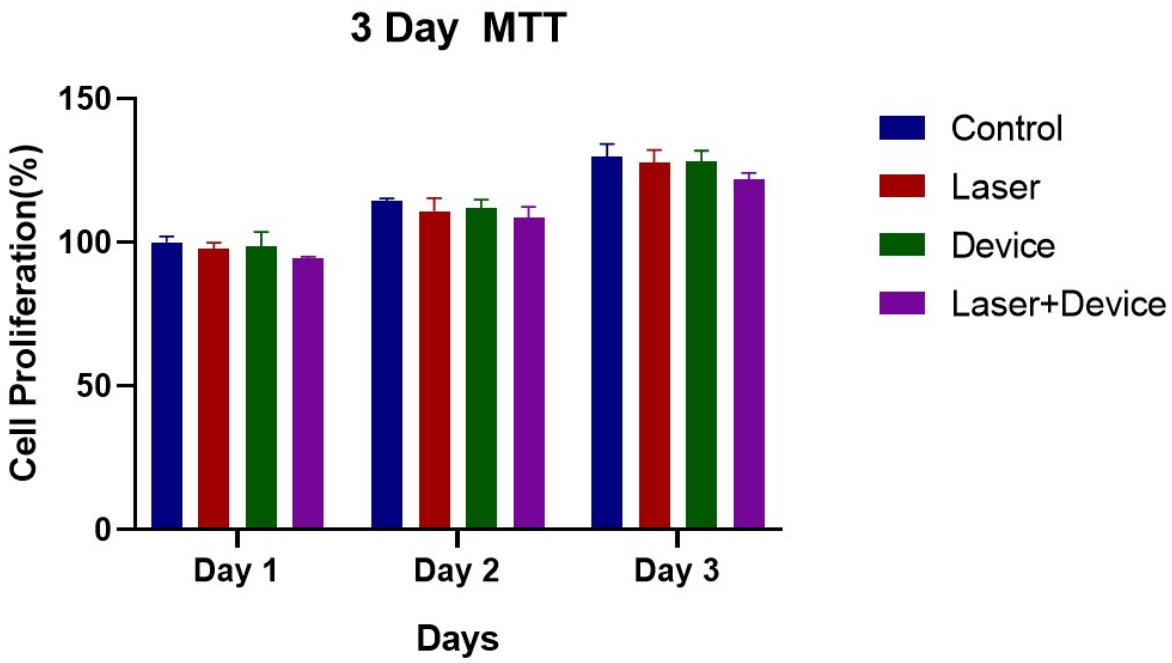

Figure S27: 3 Day MTT assay on hMSCs for different control experiment conditions.

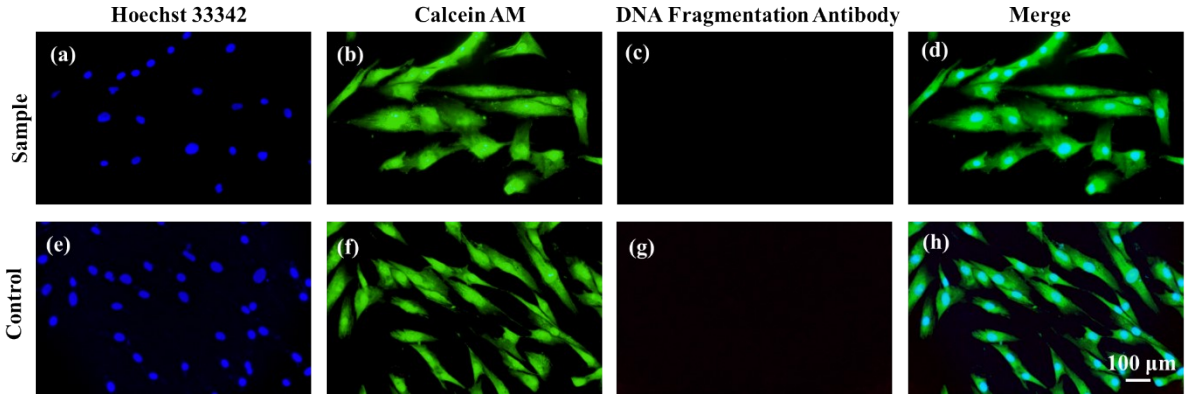

Figure S28: DNA Fragmentation analysis. (a,e) nuclear staining (blue channel), (b,f) cell viability (green channel), (c,g) cells with fragmented DNA (red channel), and (d,h) shows the merged image.

References

[1] Y. Song, Q. Tian, J. Liu, W. Guo, Y. Sun, S. Zhang, A reusable single-cell patterning strategy based on an ultrathin metal microstencil, Lab Chip 21 (2021) 1590–1597. https://doi.org/10.1039/d0lc01175d.

[2] A. Folch, B.-H. Jo, O. Hurtado, D.J. Beebe, M. Toner, Microfabricated elastomeric stencils for micropatterning cell cultures, 2000.

[3] G. R, S. Kar, M. Nagai, P.S. Mahapatra, T.S. Santra, Massively Parallel High-Throughput Single-Cell Patterning and Large Biomolecular Delivery in Mammalian Cells Using Light Pulses, Small 19 (2023) e2303053. https://doi.org/10.1002/smll.202303053.

[4] P. Shinde, A. Shinde, S. Kar, K. Illath, M. Nagai, F.G. Tseng, T.S. Santra, Ultrathin SU-8 membrane for highly efficient tunable cell patterning and massively parallel large biomolecular delivery, Lab Chip 23 (2023) 4636–4651. https://doi.org/10.1039/d3lc00244f.

[5] S. Abraham, R. Gayathri, K. Govarthanan, S. Rao, M. Nagai, T.S. Santra, Massively parallel micro-patterning of photosensitive hydrogel encapsulated single-cells to a cluster of cells and bone regeneration application, Lab Chip 25 (2025) 4735–4755. https://doi.org/10.1039/d5lc00459d.

[6] C. Tu, B. Huang, J. Zhou, Y. Liang, J. Tian, L. Ji, X. Liang, X. Ye, A microfluidic chip for cell patterning utilizing paired microwells and protein patterns, Micromachines (Basel). 8 (2017). https://doi.org/10.3390/mi8010001.

[7] Q. Luan, C. Macaraniag, J. Zhou, I. Papautsky, Microfluidic systems for hydrodynamic trapping of cells and clusters, Biomicrofluidics 14 (2020). https://doi.org/10.1063/5.0002866.

[8] Z. Dong, Y. Jiao, B. Xie, Y. Hao, P. Wang, Y. Liu, J. Shi, C. Chitrakar, S. Black, Y.C. Wang, L.J. Lee, M. Li, Y. Fan, L. Chang, On-chip multiplexed single-cell patterning and controllable intracellular delivery, Microsyst. Nanoeng. 6 (2020). https://doi.org/10.1038/s41378-019-0112-z.